Research Square

Preprints are preliminary reports that have not undergone peer review.
They should not be considered conclusive, used to inform clinical practice,
or referenced by the media as validated information.

Investigation of Sediment Thickness and Site Effects in the Guye Seismic Source Zone, Tangshan, Using the HVSR Method

Yicheng Xu
Institute of Disaster Prevention
Runyan Wang
Institute of Disaster Prevention
Jichao Huang
huangjichao@cidp.edu.cn

Institute of Disaster Prevention
Yongge Wan
Institute of Disaster Prevention
Xiaoshan Wang
Earthquake Administration of Hebei Province
Yan Zhang
Institute of Geophysics, China Earthquake Administration
Zhitong Jin
Institute of Disaster Prevention
Peiyuan Gu
Institute of Disaster Prevention

Research Article

Keywords: HVSR method, sediment thickness, site effects, Guye earthquake, Tangshan Fault Zone

Posted Date: April 1st, 2026

DOI: https://doi.org/10.21203/rs.3.rs-9197064/v1

License: This work is licensed under a Creative Commons Attribution 4.0 International License.
Read Full License

Additional Declarations: No competing interests reported.

Investigation of Sediment Thickness and Site Effects in the Guye Seismic Source Zone, Tangshan, Using the HVSR Method

Yicheng Xu[1†], Runyan Wang[1†], Jichao Huang[1*], Yongge Wan[1,2*], Xiaoshan Wang[3], Yan Zhang[4], Zhitong Jin[1], Peiyuan Gu[1]

1.Institute of Disaster Prevention, Sanhe Hebei, China, 065201

2.Hebei Key Laboratory of Earthquake Dynamics, Sanhe Hebei, China, 065201

3.Earthquake Administration of Hebei Province, Shijiazhuang Hebei, China, 050021

4.Institute of Geophysics, China Earthquake Administration, Beijing, China, 100081

*Corresponding authors: huangjichao@cidp.edu.cn (Jichao Huang);

wanyg217217@vip.sina.com.cn (Yongge Wan)

Contributing authors: fantasticity@163.com (Yicheng Xu);

yan8959853@163.com (Runyan Wang);

wxs@eq-he.ac.cn (Xiaoshan Wang);

zhangy@cea-igp.ac.cn (Yan Zhang);

jinzhitong@cidp.edu.cn（Zhitong Jin）

18875698150@163.com (Peiyuan Gu)

†These authors contributed equally to this work.

ORCID: Yicheng Xu 0009-0008-2070-3287；Runyan Wang 0009-0004-0621-5501;

Jichao Huang 0000-0002-6363-0267；Yongge Wan 0000-0002-6363-0267;

Xiaoshan Wang 0000-0002-9426-5688; Yan Zhang 0000-0002-9720-0302；

Zhitong Jin 0000-0002-0923-8563;Peiyuan Gu 0009-0002-0447-0432

Abstract Sediment thickness is an important reference for evaluating the site effects of seismic waves and a critical indicator for assessing seismic disaster losses. Based on the Horizontal-to-Vertical Spectral Ratio method (HVSR), this study calculates sediment thickness and evaluates site effects using nearly one year of ambient noise data recorded by a dense seismic array in the Guye seismic

source zone. The results show that the sediment thickness in the study area ranges from 0 to 450 m, with a significant difference between the eastern and western parts. The site amplification factor varies from 1.0 to 14.0. The site vulnerability index exhibits a spatial pattern of high values in the west and low values in the east. The western zone with thick sediments has a high risk level of 60-110, indicating a high seismic risk region for building damage. This study further reveals that the 2020 *M*s 5.1 Guye earthquake occurred in the thin-sediment zone in the northern Tangshan Fault zone. Stress diffused along the fault after the 1976 event and concentrated in the thin-sediment area to drive this earthquake. The pronounced site effects in this region further intensify the ground motion intensity. The synergistic coupling between the strong seismic source input from fault activity and site effects gives rise to anomalous ground motion, thus forming an anomalous seismic damage zone. The results of this study can provide a scientific basis for regional seismic hazard risk assessment, engineering seismic fortification, and earthquake prevention and disaster mitigation.

Keywords: HVSR method, sediment thickness, site effects, Guye earthquake, Tangshan Fault Zone

Highlights

- HVSR method realizes high-res sediment thickness inversion and site effect assessment in Guye.
- Improved HVSR processing boosts frequency estimation stability and inversion accuracy.
- Elucidate 2020 Guye *M*s5.1 coupling mechanism, verify synergistic anomalous ground motion.

1 Introduction

Earthquake damage is intricately related to source parameters, seismic wave propagation paths, and site response characteristics. Among these factors, site effects—including amplitude amplification, resonance, prolonged vibration duration, and soil liquefaction arising from seismic wave transmission through near-surface unconsolidated sediments—constitute critical contributors to building collapse and seismic disaster exacerbation. The 1989 Loma Prieta *M* 6.9 earthquake in the United States demonstrated that approximately 70% of the seismic damage was attributable to site amplification effects (Holzer, 1994). Furthermore, shallow loose soil deposits govern seismic site response characteristics, leading to differential damage in adjacent areas during the same earthquake (Ansal et al., 2001). A typical example is the 1985 Michoacán *M* 8.1 earthquake, which caused severe destruction in Mexico City—located about 400 km from the epicenter and underlain by approximately

2.5 km of sediments—resulting in up to 10,000 fatalities. In contrast, towns built on volcanic bedrock closer to the epicenter sustained only minor losses (Flores-Estrella et al., 2007). The 2002 Hualien *M*7.5 earthquake in Taiwan inflicted severe damage on the Taipei Basin (characterized by thick sediments and located approximately 110 km from the epicenter), whereas the epicentral area suffered relatively minor damage (Wang et al., 2012; Yu, 2016). These cases vividly demonstrate that the thickness and structure of sedimentary layers are primary factors controlling site effects and play a crucial role in investigating the spatial variability of seismic damage.

The *M*s 5.1 Guye earthquake on July 12, 2020, represents the largest seismic event in the Tangshan region in recent years. Its epicenter is located within the aftershock zone of the 1976 Tangshan *M*s 7.8 earthquake, approximately 28 km from the mainshock's epicenter and 26 km from the epicenter of the Luanxian *M*s 7.1 earthquake. Previous research in the Guye region is much less extensive than in the main Tangshan seismic zone, and systematic surveys of sediment thickness are notably lacking. However, sediment thickness is a critical parameter influencing site amplification of ground motion and is essential for accurately assessing the seismic vulnerability of infrastructure. Traditional borehole surveys often fail to penetrate the entire stratigraphic sequence, while active-source shallow seismic reflection and refraction surveys are prohibitively expensive. The Horizontal-to-Vertical Spectral Ratio (HVSR) method, proposed by Nakamura (1989, 2000), utilizes the spectral ratio between the horizontal and vertical components of ambient noise recordings to estimate a site's predominant frequency and amplification factor. Since it been put forward, this method has been extensively applied in site characterization, for probing buried structures and sedimentary basins, and for estimating sediment thickness (Ibs-von Seht and Wohlenberg, 1999; Parolai et al., 2002; SESAME, 2004; Chen et al., 2008; Walling et al., 2009; Hunter and Crow, 2012; Peng et al., 2020).

Notably, previous studies have not established quantitative relationships between the activity of the Tangshan Fault Zone and site effects, resulting in insufficient capability to identify anomalous seismic damage zones. Therefore, this study utilizes a dense seismic array deployed for aftershock monitoring in the Guye region to obtain high-resolution spatial distributions of sediment thickness, site amplification factor, and site vulnerability index in the Guye seismic source zone using the HVSR method. We subsequently analyze site effects to provide recommendations for seismic building code implementation and to advance seismic risk assessment and hazard mitigation efforts in the region.

2 Tectonic Setting

The Tangshan area is located at the junction between the southern margin of the eastern segment of the Yanshan Fold Belt and the Jilu Block Block, with a very complex tectonic setting (Gao et al., 1995). The Guye seismic source region (117.75°E–119.28°E, 39.64°N–39.88°N) has been a high-frequency seismic zone in Tangshan to date. It borders the Yanshan Uplift margin to the north, lies on the boundary of the North China Rift Basin to the south, and is situated on the northern segment of the Tangshan Fault zone, close to active fault belts. The region is confined within a structurally intricate rhombic block bounded by four Quaternary active faults. As illustrated in Figure 1, the Ninghe-Changli Fault, Zhenzizhen Fault, Fengtai-Yejituo Fault, Luanxian-Leting Fault, and Jiyunhe Fault collectively delineate a rhombic domain encompassing the study area. In addition to these bounding structures, two NE-trending fault systems—the Tangshan Fault Zone and the Lulong Fault—traverse the study region. The Tangshan Fault Zone, occupying the central portion of the rhombic block along its obtuse-angle diagonal, constitutes a complex fault-fold structural system comprising three subparallel NNE–NE-trending faults: the Tangshan-Douhe Fault, the Weishan-Changshan Fault, and the Tangshan-Guye Fault (Guo et al., 1977).

The epicenter of the 12 July 2020 *M*s 5.1 Guye earthquake lies in the northern segment of the Tangshan Fault Zone. Despite its moderate magnitude, this earthquake produced strong ground shaking that was clearly felt throughout Beijing and Tianjin, with anomalous seismic intensity distribution. The maximum instrumental intensity was recorded near the epicenter; however, the intensity V zone was asymmetrically distributed toward the southeast and north (Li et al., 2020). Additionally, the Tanggu–Ninghe–Baodi triangular area of Tianjin, despite being far from the epicenter, exhibited anomalously enhanced ground motion (Wen et al., 2020), indicating significant site amplification effects. These site-dependent damage variations and intensity anomalies cannot be fully quantified by conventional tectonic and source parameters alone. A reasonable interpretation requires integrated analysis of near-surface sediment thickness and site amplification effects, which motivates the present study with clear practical and scientific significance.

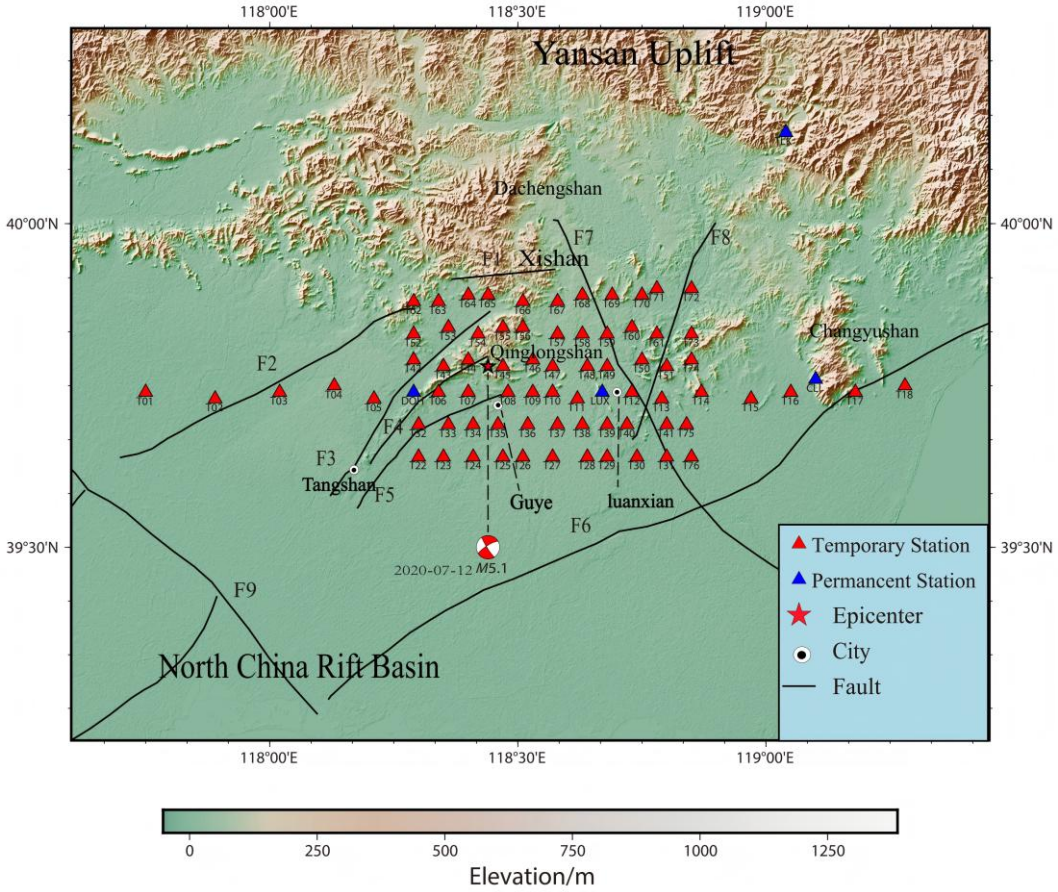


Figure 1 Distribution of seismic stations and tectonic background.F1: Zhenzizhen Fault, F2: Fengtai-Yeituo Fault, F3: Tangshan-Douhe Fault, F4: Weishan-Changshan Fault, F5:Tangshan-Guye Fault, F6: Ninghe-Changli Fault, F7: Luanxian-Leting Fault, F8: Lulong Fault, F9: Jiyunhe Fault

3 Methodology and Data

3.1 HVSR Method

The site resonance frequency is a critical parameter for characterizing near-surface sediment thickness and evaluating site effects. Accurate determination of this frequency holds significant engineering and scientific implications for ground motion prediction, site classification, and seismic risk assessment. The Horizontal-to-Vertical Spectral Ratio (HVSR) method has been proposed as a popular technique for site response evaluation, sediment thickness inversion, and detection of buried structures, owing to its advantages of not requiring active seismic sources, single-station operability, cost effectiveness, and high efficiency. Originally proposed by Nogoshi and Igarashi (1971) and subsequently systematized and popularized by Nakamura (1989), this method has gradually evolved to

a standardized technical workflow. Numerous theoretical and experimental studies have demonstrated that, in areas with high impedance contrast, the HVSR peak frequency essentially equals with the site resonance frequency (Bard, 1999; Lachetl and Bard, 1994; Lermo and Chávez-García, 1994). This fundamental physical relationship provides a robust theoretical foundation and viable technical pathway for quantitatively calculating near-surface sediment thickness and assessing site amplification effects via HVSR peak frequency analysis.

Conventional methods typically assume that the HVSR peak frequency f_0 follows a normal distribution. This assumption inherently allows for a probability of $f_0 < 0$ Hz, which is physically meaningless. Furthermore, its reciprocal period $T_0 = 1/f_0$ follows a reciprocal normal distribution, whose mean and variance are not exist, leading to statistically ambiguous parameters for T_0. This study employs the lognormal distribution and frequency-domain window-rejection algorithm proposed by Cox et al. (2020) to process HVSR curves. This algorithm enables seamless conversion between frequency and period domains, automatically identifying and rejecting anomalous windows arising from noise, poor sensor coupling, or other artifacts, thereby enhancing the stability and consistency of f_0 estimation.

In HVSR data processing, assuming that amplitudes in each frequency time window follow a lognormal distribution, median amplitudes at each frequency are computed using data from different time windows and concatenated to obtain the median HVSR curve. By collecting f_0 from each time window, a sample set is formed, denoted as $f_{0,i}$, where i represents the ith window. The mean μf_0 and standard deviation σf_0 of this sample set can then be calculated. It should be noted that the peak frequency $f_{0,mc}$ of the median curve typically does not equal μf_0, as illustrated in Figure 2. If f_0 follows a lognormal distribution (LD), then lnf_0 follows a normal distribution (ND), with its mean and standard deviation denoted as μlnf_0 and σlnf_0, respectively. This relationship can be expressed by Equation (1):

$$ln(f_0) \sim ND(\mu \ln f_0, \sigma \ln f_0) \leftrightarrow f_o \sim LD(\mu \ln f_0, \sigma \ln f_0) \quad (1)$$

$\sim$ denotes a random variable following a specified distribution; $\leftrightarrow$ is the symbol for interconversion.

$$T_0 = \frac{1}{f_0} \qquad ln(T_0) = -ln(f_0) \tag{2}$$

Since $ln(f_0)$ follows a normal distribution, $-ln(f_0)$ ($ln(T_0)$) also follows a normal distribution, with its mean and standard deviation denoted as $-\mu lnf_0$ and σlnf_0 , respectively. Because the lognormal distribution of f_0 and the normal distribution of lnf_0 are interchangeable, therefore

$$ln(T_0) \sim ND(-\mu \ln f_0, \sigma \ln f_0) \leftrightarrow T_o \sim LD(-\mu \ln f_0, \sigma \ln f_0) = LD(\mu \ln T_0, \sigma LnT_0) \tag{3}$$

T_0 also follows a lognormal distribution, with its statistics obtainable from those of f_0 .

For a lognormally distributed f_0 , the distribution parameters in log space should be inverse-transformed back to physical space (frequency) to obtain representative values with original units. One such "inverse transformation" yields the lognormal median of f_0 , denoted as LMf_0 in this study. LMf_0 is the parameter that statistically characterizes the mean/expectation of f_0 . The relationship between LMf_0 and μlnf_0 is:

$$LMf_0 = \mathrm{e}^{\mu \ln f_0} \tag{4}$$

To effectively suppress anomalous noise and ensure computational accuracy, the frequency-domain window-rejection algorithm is employed. All peak frequencies $f_{0,\mathrm{i}}$ are collected, and extreme HVSR window $f_{0,\mathrm{i}}$ values are eliminated through multiple iterations, bringing the lognormal median LMf_0 as close as the median curve peak $f_{0,\mathrm{mc}}$ while avoiding manual subjective window rejection. After culling, HVSR curves from all time windows stabilize at f_0 , and the median curve peak $f_{0,\mathrm{mc}}$ is taken as the fundamental resonance frequency of the sedimentary layer beneath the station (Cox et al., 2020).

To obtain HVSR curves, three-component ambient noise data (NS, EW, V) recorded at each station are first partitioned into time windows longer than 10 times the site natural period (SESAME, 2004) and further divided into multiple windows. The Fourier amplitude spectrum ratio between horizontal and vertical components is then calculated for each time window. We adopt the geometric mean (GM) method recommended by SESAME (2004) to compute the horizontal component of the

HVSR curve $\mathrm{GM} = \sqrt{NS \square EW}$, as this approach has a long history in ground motion processing and is consistent with the lognormal distribution assumption for ground motion intensity measures (Haghshenas et al., 2008; Pileggi et al., 2011). The Fourier amplitude spectrum ratio between horizontal and vertical components for each time window is:

$$\mathrm{HVSR}(f) = \sqrt{\frac{\mathrm{NS}\ (f) \bullet \mathrm{EW}(f)}{\mathrm{V}(f)}} \tag{5}$$

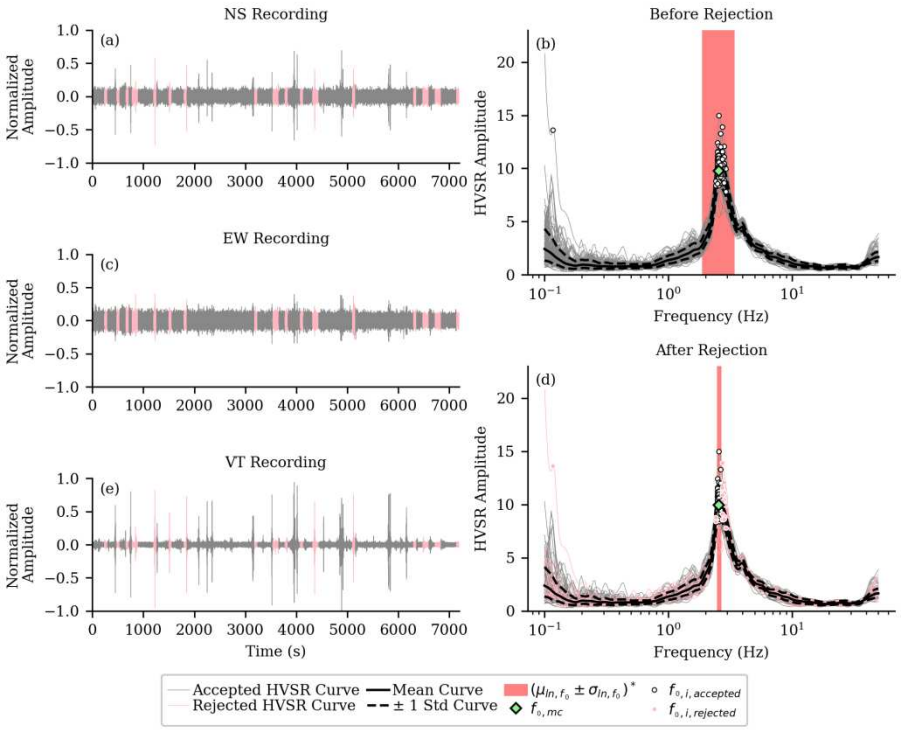


Figure 2 Schematic diagram of the lognormal distribution and frequency-domain window-rejection algorithm.Calculation results for station T13 using data from 02:00-04:00 on August 27, 2020. (a), (c), and (e) Three-component seismic records; grey (accepted) and pink (rejected) indicate accepted and rejected time windows, respectively. (b) HVSR curves before applying the rejection algorithm; grey curves show all HVSR curves, open circles $f_{0,\mathrm{i}}$ denote the peak frequency of each curve, and green diamonds $f_{0,\mathrm{mc}}$ represent the peak frequency of the median curve. (d) HVSR curves after applying the frequency-domain window-rejection algorithm; pink circles $f_{0,\mathrm{i}}$ denote peak frequencies of rejected HVSR curves, and green diamonds $f_{0,\mathrm{mc}}$ represent the peak frequency of the median curve after culling.

3.2 Sediment Thickness Calculation and Site Effect Assessment

Assuming a uniform and isotropic shallow subsurface velocity structure, the sediment thickness $h(\mathrm{m})$ beneath a station is proportional to the quarter-wavelength λ of the fundamental resonant seismic wave in the sedimentary layer, with higher-order resonances occurring at odd multiples (Ibs-von Seht and Wohlenberg, 1999):

$$h = \frac{n\lambda}{4} n = 1,3,5.... \tag{6}$$

$$\lambda = \frac{v_s}{f_r} \tag{7}$$

where $v_s(\mathrm{m/s})$ is the average S-wave velocity of the sediment layer and f_r (Hz) is the resonance frequency. Combining Equations (6) and (7), we obtain:

$$f_r = \frac{nv_s}{4h} n = 1,3,5.... \tag{8}$$

When $n = 1$, the resonant frequency is the fundamental resonant frequency f_0 (Hz) :

$$f_0 = \frac{v_s}{4h} \tag{9}$$

Transforming Equation (9) yields the sediment thickness formula:

$$h = \frac{v_s}{4f_0} \tag{10}$$

Given the shear wave velocity, the sediment thickness can be derived from the peak frequency of the HVSR curve (Ibs-von Seht and Wohlenberg, 1999; Parolai et al., 2002).

The site amplification factor A is defined as the amplitude at the HVSR curve peak frequency f_0 (fundamental resonant frequency). The site vulnerability index K, first introduced by Nakamura (1997), is derived from the correlation between surface shear strain and the depth and shear wave velocity of loose sediment layers. Assuming a constant sediment layer velocity and a dynamic conversion efficiency of 60%, its approximate calculation formula is:

$$K = \frac{A^2}{f_0} \tag{11}$$

The site vulnerability index K is a parameter characterizing the destructive capacity of seismic hazards on surface structures. To evaluate site safety in the study area under potential earthquake

disasters, after obtaining the site amplification factor A and its corresponding peak frequency f_0, the site vulnerability index K for the study area is calculated using Equation (11).

3.3 Data

The seismic network in the Guye area of Tangshan began operation in August 2020. As shown in Figure 1,the network consists of 73 temporary seismic stations and 4 permanent stations, among which 55 temporary stations are short-period seismometers arranged in a rectangular array, 18 temporary stations are broadband seismometers deployed in a linear strip in the center of the rectangle, and all 4 permanent stations are equipped with broadband seismometers. The network covered a maximum east-west extent of approximately 131 km and a minimum east-west extent of approximately 46.3 km, with a north-south aperture of approximately 27 km. The average inter-station spacing was approximately 4.6 km in the east-west direction and 5.4 km in the north-south direction. All data loggers were set to a uniform sampling rate of 100 Hz. The relatively dense deployment of this seismic network in the Guye region, recording continuously for nearly one year (August 2020–July 2021), provided reliable waveform data of ambient seismic noise for HVSR analysis in this study.

4 Results

4.1 Data Screening and Calculation Results

To ensure the reliability of HVSR calculations, this study employs a dual-dimension quality assessment system based on Reliability and Clarity according to SESAME standards (SESAME, 2004). Reliability evaluates HVSR curve stability through three criteria: the frequency-window length condition, the significant cycles condition, and the standard deviation condition. Clarity assesses peak significance and identifiability via six criteria: low-frequency amplitude, high-frequency amplitude, peak amplitude, frequency stability, frequency standard deviation, and amplitude standard deviation. Data are deemed acceptable only if all three Reliability criteria are satisfied and at least five of the six Clarity criteria are met. Furthermore, the total number of satisfied criteria across both dimensions positively correlates with data quality; a higher count indicates greater HVSR curve stability and peak significance, yielding more reliable frequency identification results.

The seismometers employed in this study were calibrated prior to dense array deployment. To mitigate interference from anthropogenic background noise, nighttime data were selected for HVSR calculation. Using May 1, 2021 as a sample day, the periods 02:00-04:00 and 04:00-06:00 Beijing

Time were evaluated with identical control parameters (e.g., window length, smoothing). The period exhibiting the highest qualification rate was selected. Comparative results (Table 1) demonstrate that the 02:00-04:00 period achieved a qualification rate of 75.71%, significantly exceeding the 68.57% rate for 04:00-06:00. Furthermore, the total number of satisfied criteria for 02:00-04:00 was 562, superior to the 550 for the latter period. Consequently, the 02:00-04:00 time window was adopted as the study period (Table 1).

Table 1 HVSR Data Qualification Status for the 02:00-04:00 and 04:00-06:00 Periods

Station 02:00-04:00	Maximum amplitude	f_0 (Hz)	Reliability result	Clarity result	Total result	Station 02:00-04:00	Maximum amplitude	f_0 (Hz)	Reliability result	Clarity result	Total result
CLI	1.69	44.13	3	2	5	CLI	1.76	44.13	3	2	5
DOH	2.51	33.32	3	6	9	DOH	2.26	32.29	3	4	7
LUX	1.40	15.26	3	3	6	LUX	2.44	0.11	2	5	7
T01	3.69	50.00	3	3	6	T01	3.96	0.34	3	3	6
T02	3.95	0.35	3	5	8	T02	4.16	0.37	3	6	9
T05	4.87	0.15	2	3	5	T05	16.53	0.11	2	5	7
T06	7.61	7.92	3	6	9	T06	8.36	7.92	3	6	9
T07	8.32	4.51	3	6	9	T07	9.42	0.11	2	3	5
T08	4.66	2.13	3	6	9	T08	4.97	2.20	3	6	9
T09	5.34	1.14	3	6	9	T09	5.28	1.11	3	6	9
T10	5.59	1.42	3	5	8	T10	5.35	1.42	3	5	8
T11	10.54	1.38	3	6	9	T11	10.58	1.38	3	6	9
T12	10.84	2.34	3	6	9	T12	10.09	2.34	3	5	8
T13	9.50	2.66	3	5	8	T13	9.66	2.66	3	6	9
T14	2.58	3.41	3	5	8	T14	2.43	3.41	3	4	7
T15	5.19	1.88	3	6	9	T15	5.02	1.88	3	6	9
T16	6.64	1.56	3	6	9	T16	6.59	1.51	3	6	9
T17	5.15	45.53	3	5	8	T17	5.65	45.53	3	3	6
T18	6.50	1.38	3	6	9	T18	6.18	1.42	3	5	8
T22	5.35	1.22	3	6	9	T22	4.75	1.22	3	5	8
T23	7.79	1.38	3	6	9	T23	7.70	1.38	3	6	9
T24	4.62	1.14	3	6	9	T24	5.15	1.11	3	6	9
T25	6.87	1.18	3	6	9	T25	5.38	1.18	3	6	9
T26	5.60	0.81	3	6	9	T26	4.90	0.84	3	5	8
T27	4.16	0.84	3	6	9	T27	3.91	0.81	3	6	9
T28	5.08	1.01	3	6	9	T28	5.80	1.01	3	4	7
T29	7.32	0.69	3	6	9	T29	7.85	0.69	3	6	9
T30	4.98	0.74	3	6	9	T30	2.99	0.74	3	4	7
T31	6.36	1.25	3	6	9	T31	5.89	1.29	3	6	9
T32	7.35	4.38	3	6	9	T32	7.03	4.38	3	6	9
T33	7.64	2.13	3	6	9	T33	7.18	2.20	3	6	9
T34	5.06	2.00	3	5	8	T34	4.62	1.94	3	5	8
T35	9.52	1.66	3	6	9	T35	8.04	1.66	3	6	9
T36	3.50	1.04	3	4	7	T36	2.37	1.14	3	5	8
T37	5.22	1.11	3	6	9	T37	4.93	1.18	3	6	9
T38	3.14	0.79	3	4	7	T38	2.15	1.07	3	3	6
T39	6.74	1.14	3	6	9	T39	6.17	1.18	3	6	9
T40	7.33	1.56	3	6	9	T40	7.04	1.56	3	6	9
T41	5.73	1.66	3	6	9	T41	5.39	1.66	3	6	9
T42	6.60	2.49	3	6	9	T42	6.41	2.49	3	6	9
T44	1.83	50.00	3	1	4	T44	1.86	0.14	2	3	5
T45	6.65	6.78	3	6	9	T45	5.14	6.78	3	6	9
T46	8.20	2.20	3	6	9	T46	8.49	2.20	3	6	9
T47	5.42	1.29	3	6	9	T47	5.50	1.29	3	6	9
T51	4.02	3.10	3	6	9	T51	3.91	3.20	3	6	9
T52	1.31	24.38	3	1	4	T52	1.32	24.38	3	1	4
T53	3.09	1.38	3	6	9	T53	3.36	1.42	3	6	9
T54	1.87	32.29	3	2	5	T54	1.68	33.32	3	2	5
T55	2.23	27.62	3	4	7	T55	2.13	27.62	3	4	7
T56	1.69	50.00	3	1	4	T56	1.90	50.00	3	2	5
T57	4.42	1.07	3	6	9	T57	4.20	1.07	3	5	8
T59	5.78	1.14	3	4	7	T59	5.44	1.18	3	5	8
T60	4.11	3.63	3	6	9	T60	4.36	3.63	3	6	9
T61	7.67	12.26	3	6	9	T61	7.26	12.26	3	6	9
T62	6.56	5.62	3	6	9	T62	6.17	5.80	3	6	9
T63	4.64	2.42	3	4	7	T63	4.82	2.34	3	5	8
T64	5.90	4.96	3	6	9	T64	5.88	4.96	3	6	9
T65	3.28	10.49	3	6	9	T65	2.94	10.49	3	5	8
T66	1.59	45.53	3	1	4	T66	1.25	42.77	3	1	4
T67	9.14	2.20	3	6	9	T67	9.00	2.20	3	6	9
T68	3.12	10.82	3	3	6	T68	2.88	0.11	2	4	6
T69	13.70	3.10	3	5	8	T69	14.12	3.10	3	5	8
T70	10.84	1.83	3	6	9	T70	10.31	1.83	3	6	9
T71	5.87	3.01	3	6	9	T71	5.77	3.01	3	6	9
T72	3.20	1.71	3	6	9	T72	1.90	1.83	3	3	6
T73	1.42	8.97	3	1	4	T73	1.42	8.70	3	2	5
T74	1.76	33.32	3	2	5	T74	2.05	44.13	3	3	6
T75	6.05	1.29	3	6	9	T75	5.49	1.25	3	6	9
T76	5.26	1.01	3	5	8	T76	4.66	1.01	3	4	7
TLK	3.01	33.32	3	6	9	TLK	2.87	33.32	3	6	9
					562						550

To ensure the final results are reliable, we conducted comprehensive screening for station stability and overall data quality. Qualified data must satisfy two requirements: (1) Clarity criteria ≥5 and all

Reliability criteria satisfied; (2) Clear peaks in HVSR curves calculated for the 02:00-04:00 period. After data screening, 66 stations with qualified data were selected (Table 2). For stations with ≥4 valid records, the highest and lowest frequency values were removed and the remaining values averaged to represent the frequency beneath the station. For stations with <4 valid records, the simple average was used. The same procedure was applied to obtain the amplification factor A at each station. The average shear wave velocity of shallow sediments in this region was set to 500 m/s (Liu et al., 2011a,b; Wang and Li, 2018). Long (2010) drilled boreholes in the western part of the study area (118°08′E, 39°36′N) and found denser gravel layers at the base of the Yangliuqing Formation in the middle Pleistocene. When hard interlayers such as gravel or cemented sand layers exist within Quaternary strata, their shear wave velocity may reach 500-700 m/s (Su et al., 2020). Therefore, we adopted an intermediate value of 600 m/s for the western region (stations T01, T02, T03). Using Equations (10) and (11), the sediment thickness and site vulnerability index K were estimated for each station. Ultimately, 66 stations met all criteria, with results presented in Table 2.

Table 2 Qualified stations, data and computation results in the Guye seismic source zone, Tangshan

Station	Qualified data	Longitude (°)	Latitude (°)	Site amplification factor	f_0 (Hz)	Sediment thickness(m)	site vulnerability index
CLI	3	119.1	39.76	2.11	35.10	3.56	0.13
T01	60	117.75	39.74	6.06	0.33	454.55	111.28
T02	75	117.89	39.73	5.88	0.34	441.18	101.69
T03	13	118.02	39.74	5.26	0.34	441.18	81.38
T04	57	118.13	39.75	5.85	0.95	131.58	36.02
T05	5	118.21	39.73	5.44	0.98	127.55	30.20
T06	105	118.34	39.74	7.15	7.69	16.25	6.65
T07	74	118.4	39.74	10.78	4.59	27.23	25.32
T08	81	118.48	39.74	4.72	2.19	57.08	10.17
T09	186	118.53	39.74	5.92	1.11	112.61	31.57
T10	36	118.57	39.74	5.82	1.34	93.28	25.28
T11	172	118.62	39.73	10.71	1.31	95.42	87.56
T12	25	118.73	39.74	10.68	2.32	53.88	49.16
T13	96	118.79	39.73	9.77	2.60	48.08	36.71
T14	21	118.87	39.74	2.60	3.34	37.43	2.02
T15	58	118.97	39.73	5.29	1.81	69.06	15.46
T16	84	119.05	39.74	7.47	1.47	85.03	37.96
T17	5	119.18	39.74	3.55	46.97	2.66	0.27
T18	15	119.28	39.75	6.87	1.38	90.58	34.20
T22	50	118.3	39.64	10.01	1.24	100.81	80.81
T23	128	118.35	39.64	7.97	1.38	90.58	46.03
T24	125	118.41	39.64	4.71	1.1	113.64	20.17
T25	123	118.47	39.64	6.5	1.17	106.84	36.11
T26	89	118.51	39.64	5.17	0.85	147.06	31.45
T27	86	118.57	39.64	4.23	0.83	150.60	21.56
T28	84	118.64	39.64	5.64	0.96	130.21	33.14
T29	3	118.68	39.64	5.98	0.72	173.61	49.67
T30	97	118.74	39.64	6.07	0.74	168.92	49.79
T31	116	118.8	39.64	6.02	1.29	96.90	28.09
T32	100	118.3	39.69	8.40	4.40	28.41	16.04
T33	76	118.36	39.69	7.55	2.17	57.60	26.27
T34	112	118.41	39.69	5.06	1.95	64.10	13.13
T35	137	118.46	39.69	10.13	1.67	74.85	61.45
T36	100	118.52	39.69	6.18	0.92	135.87	41.51
T37	75	118.58	39.69	5.84	1.13	110.62	30.18
T38	90	118.63	39.69	5.03	0.79	158.23	32.03
T39	67	118.68	39.69	6.11	1.18	105.93	31.64
T40	53	118.72	39.69	6.93	1.56	80.13	30.79
T41	76	118.8	39.69	5.87	1.63	76.69	21.14
T42	95	118.29	39.79	6.55	2.51	49.80	17.09
T45	40	118.47	39.78	4.38	6.49	19.26	2.96
T46	47	118.53	39.79	8.87	2.14	58.41	36.76
T47	68	118.57	39.78	5.59	1.33	93.98	23.49
T48	7	118.64	39.78	1.39	1.04	120.19	1.86
T49	97	118.68	39.78	6.99	1.19	105.04	41.06
T50	20	118.75	39.79	6.89	3.66	34.15	12.97
T51	23	118.8	39.78	4.36	3.21	38.94	5.92
T52	1	118.29	39.83	2.52	7.92	15.78	0.80
T55	4	118.47	39.84	2.30	25.55	4.89	0.21
T57	36	118.58	39.83	4.68	1.06	117.92	20.66
T58	10	118.63	39.83	6.15	1.07	116.82	35.35
T59	55	118.68	39.83	5.79	1.13	110.62	29.67
T60	22	118.73	39.84	4.26	3.58	34.92	5.07
T61	24	118.78	39.83	5.45	12.82	9.75	2.32
T62	93	118.29	39.88	6.91	5.62	22.24	8.50
T63	78	118.34	39.88	4.97	2.34	53.42	10.56
T64	80	118.4	39.89	6.21	4.91	25.46	7.85
T65	32	118.44	39.89	3.92	9.92	12.60	1.55
T67	46	118.51	39.88	10.37	2.14	58.41	50.25
T68	2	118.58	39.88	4.39	6.17	20.26	3.12
T69	143	118.63	39.89	14.06	3.11	40.19	63.56
T70	31	118.69	39.89	9.47	1.84	67.93	48.74
T71	124	118.75	39.89	7.06	2.93	42.66	17.01
T74	1	118.78	39.9	3.3	38.95	3.21	0.28
T75	17	118.84	39.69	6.02	1.26	99.21	28.76
T76	23	118.85	39.64	5.09	1.03	121.36	25.15

4.2 Predominant Frequency and Tectonic Response

To more intuitively compare predominant frequencies at different measurement points within the region, we employed an interpolation method to generate a predominant frequency distribution map

(Figure 3). The study area exhibits a clear zonal pattern, with predominant frequencies generally low in the south and high in the east and north. High predominant frequencies (>10 Hz) are tightly clustered in the mountainous northeastern part of the study area, where bedrock outcrops occur. These outcrops correspond geologically to the southern margin of the Yanshan Uplift, and steep frequency gradients are observed along the edges of the hard rock exposure zones. Low predominant frequencies (<2 Hz) are distributed across the extensive southern and western regions of the study area, which are geologically situated at the margin of the Tangshan Depression. Station T55 displays medium-to-high predominant frequencies (approximately 10–20 Hz), located at the superposition of the Weishan–Changshan Fault and the Qinglongshan Anticline. The thrust component of the fault uplifted the hanging-wall bedrock, forming a rigid protrusion. Although the sediment thickness is only 4.89 m, it exhibits high predominant frequencies, revealing that active faults influence shallow velocity structure through thrust uplift of bedrock, thereby generating a high-frequency anomaly associated with thin sedimentary layers.

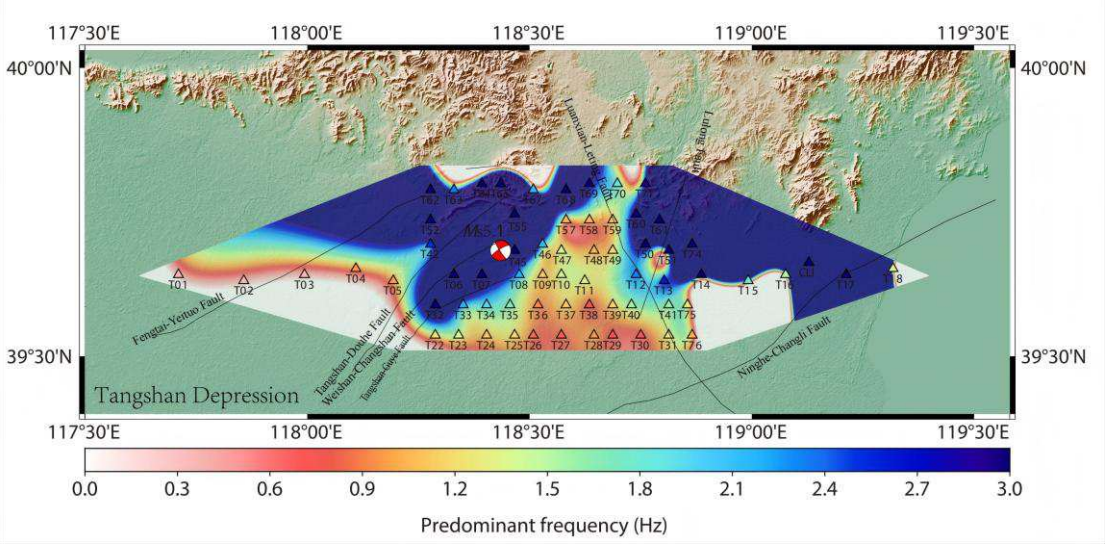


Figure 3 Predominant frequency distribution map of the study area

4.3 Sediment Thickness Distribution

The sediment thickness in the study area ranges from 0–450 m, with maximum values of approximately 450 m in the western depression adjacent to the Tangshan Depression. Minimum thickness occurs in the northeastern hills, approaching zero at bedrock outcrops near the southern margin of the Yanshan Uplift, with variations consistent with topography and surface geology (Figure 4). Figure 5 presents a Quaternary thickness contour map based on sparse drilling data from Liu et al. (1982). Our results are generally consistent with previous geological surveys, both exhibiting a spatial

distribution of thinner deposits in the northeastern parts and thicker deposits in the southwestern parts of the study area. This study provides finer-scale details whose fluctuations correlate with topography and subsurface structure, though inconsistencies appear at the deepest western locations. The sediment thickness results for the Tangshan region obtained by Bao et al. (2019) using the dense seismic station method exhibit better agreement with those of this study at the deepest sites in the western part of the study area. Meanwhile, their study also reveals that the thickness of the Quaternary strata measured via borehole drilling is greater than the sedimentary layer thickness calculated from the HVSR method in the western study area, and this phenomenon will be further elaborated in the discussion section.

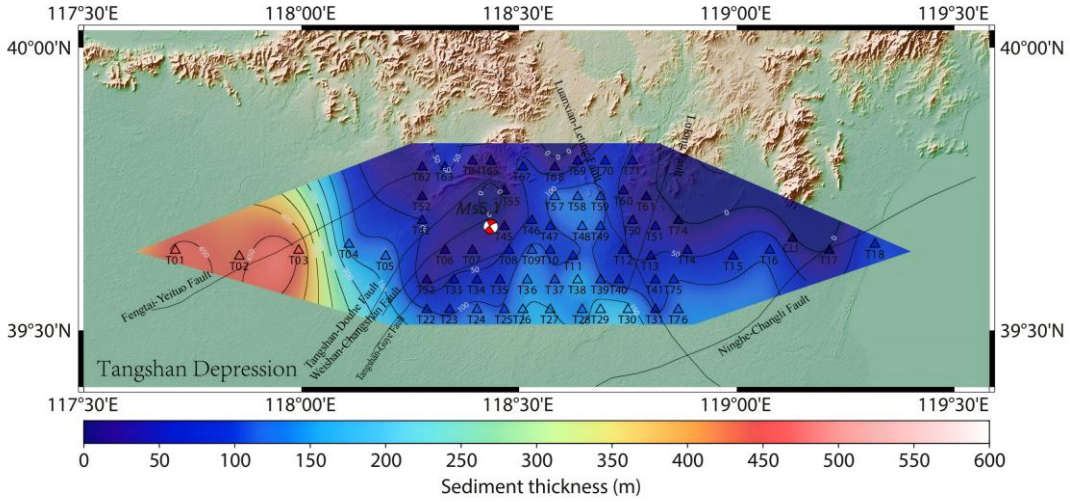


Figure 4 Sediment thickness map of the study area

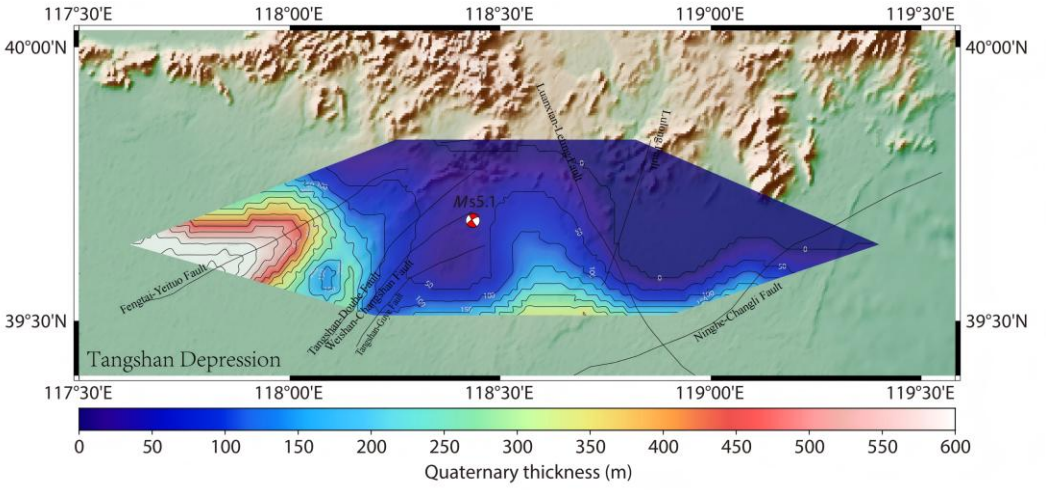


Figure 5 Quaternary Thickness Map of the Study Area (Liu et al., 1982)

4.4 Site Effects Analysis

The site amplification factor serves as a critical metric for quantifying the amplification of ground motion intensity by a site. According to SESAME (2004), HVSR-derived amplification factors underestimate actual site amplification, and HVSR peak amplitudes should therefore be regarded as conservative lower bounds. Consequently, this study uses HVSR peak amplitudes as conservative estimates of site amplification factors, providing clear physical significance and engineering reference value.

Study area amplification factors range from 1.0-14.0, exhibiting significant spatial heterogeneity (Figure 6). The northeastern region shows the lowest values of 1.0-2.0, where bedrock outcrops or the overburden is extremely thin, resulting in high site rigidity and limited amplification. Most areas exhibit intermediate amplification of 4.0-7.0, corresponding to regions with moderate sediment thickness and moderate site amplification effects. In localized zones, amplification factors exceed 7.0, reaching up to 14.0, indicating pronounced site amplification.

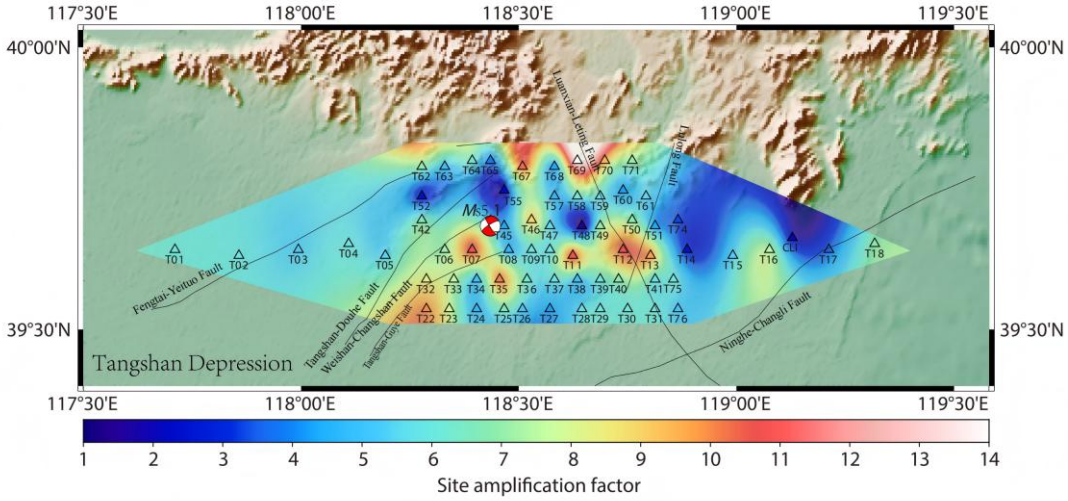


Figure 6 site amplification factor map of the study area

Nakamura (1997) introduced the site vulnerability index K as a physical parameter for quantifying site vulnerability index. A higher value of this index indicates that buildings on the site are more vulnerable to damage. Statistical results indicate that when K > 20, buildings are likely to be damaged when an earthquake occurs, surface structures are likely to be damaged.

The study area exhibits pronounced spatial variation in K values, displaying a zonal characteristic of high values in the west and low values in the east that is highly coupled with sediment thickness, aquifer architecture, and fluid pressure gradients (Figure 7). In the Tangshan region, sediment thickness increases progressively from north to south, aquifers transition from single to

multiple layers with increasing individual thickness, and groundwater evolves from unconfined to semi-confined and confined conditions (Feng, 2013). Northeastern and northwestern parts of the study area show K values of 0-20, corresponding to bedrock outcrops or thin overburden zones with high site stiffness and relatively low seismic damage risk for buildings. Central regions exhibit K values of 20-60, indicating moderate-thickness sediments where buildings may develop cracks or localized damage during strong earthquakes. The western region records the highest K values, reaching 60-110, representing the peak vulnerability zone in the study area. Here, thick loose sediments coexist with complex multi-layer aquifers, pore liquid pressure can rise sharply during seismic loading, and amplification of ground motion combined with liquefaction risk is significant, making building structures highly vulnerable to severe damage or even collapse during earthquakes.

High porosity and high liquid saturation in thick sediment layers are key factors in the frequent triggering of secondary disasters such as sand boils and ground subsidence. Therefore, the high-K-value zone in the western region is both a high-risk area where buildings are most vulnerable to damage and a hazardous zone for secondary disasters.

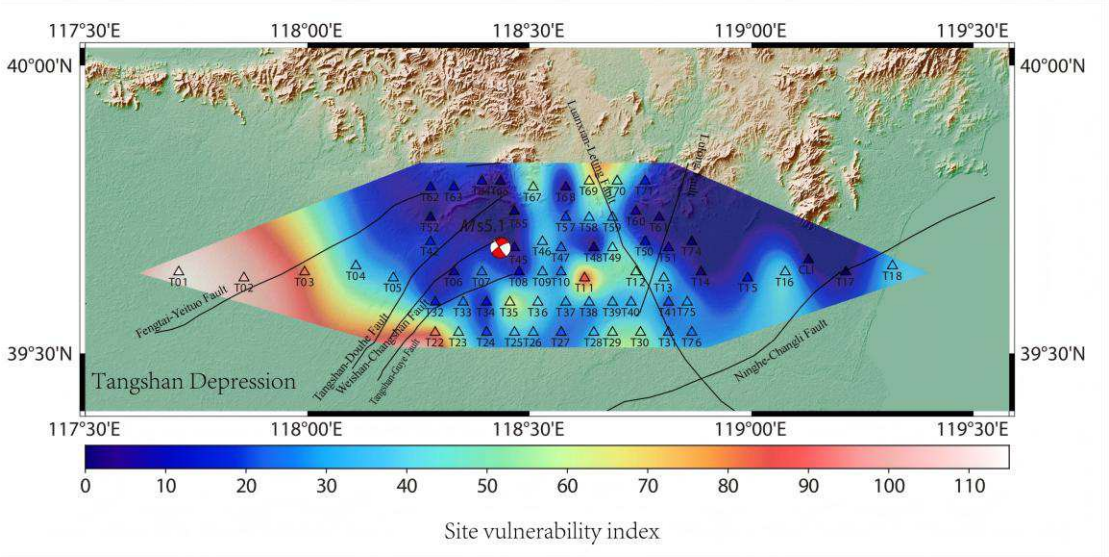


Figure 7 Site vulnerability index map of the study area

5 Discussion

5.1 Interpretation of Sediment Thickness Variations

Compared with Liu et al. (1982), both results exhibit the spatial pattern of thinner sediments in the north and east, and thicker deposits in the south and west. However, the western thickness obtained in

this study is significantly smaller than the Quaternary thickness reported by drilling data. This discrepancy can be explained from the following aspects:

Different measurement principles. The HVSR method detects the thickness of the loose sediment layer in terms of seismic wave response—that is, the strata that contribute to seismic amplification effects—based on the division of physical interfaces with seismic impedance contrasts. In contrast, the Quaternary thickness in geological drilling is a measure of the sedimentary record from a specific geological historical period; the scope covered by the two is not entirely identical. The fact that the sediment thickness detected by HVSR is smaller than the total Quaternary thickness may be due to the presence of dense hard layers within the Quaternary strata in the western part of the study area (Long, 2010). These hard layers have shear wave velocities far exceeding those of loose sediments, sufficient to constitute a significant seismic impedance contrast interface, causing the HVSR method to interpret it as the bedrock interface. Therefore, the "sedimentary layer" thickness detected only represents the uppermost loose layer, rather than the total thickness of the entire Quaternary stratum.

Spatial resolution differences. Previous research based on sparse drilling points with large-scale interpolation may have over-smoothed the spatial variation of sediment thickness. This study, however, employs a dense array with station spacing of 4-6 km, capable of revealing the true gradient of thickness variation. The study area lies at the edge of the Yanshan Uplift, where complex tectonics produce dramatic lateral changes in sediment thickness. Sparse drill holes may only represent local depression centers, while the dense array can capture regional average characteristics.

Despite absolute value discrepancies, the two methods exhibit good consistency in regional trends: both indicate thinner sediments in the northern and eastern parts and thicker deposits in the southern and western parts. This demonstrates that our results are reliable and provide fine-scale structural information unparalleled in previous studies.

5.2 Site Effects and Thickness Distribution

The anomalous phenomenon of maximum amplification factors occurring in moderate-thickness zones reveals a nonlinear thickness-dependent amplification mechanism of site amplification effects. Traditional empirical relationships suggest that greater sediment thickness yields stronger amplification (Nakamura, 2000), but this principle is valid only in homogeneous media. The Guye earthquake occurred within the Tangshan Fault Zone, which constitutes a complex structural belt composed of multiple faults associated with folds. These faults exhibit varied cross-sectional morphologies,

displacing deep structures at different levels and displaying flower structure characteristics. Shallow seismic reflection profiles reveal abundant reflectors with strong reflection energy, good lateral continuity, and clear interface undulations—features typical of sedimentary layer reflections(Liu et al., 2011c). Gravel-rich hard interlayers within the thick sediment zone in the western study area create multiple reflection interfaces, causing seismic energy to be repeatedly partitioned and dissipated within complex layered structures, thereby reducing HVSR peak amplitudes. Furthermore, the high damping characteristics of deep loose sediments absorb additional medium-to-high frequency seismic energy, attenuating amplification magnitude.

In contrast, moderate-thickness zones, such as Station T69, typically correspond to single homogeneous sedimentary layers without significant hard interlayer interference. With thickness approximating the quarter-wavelength of medium-high frequency seismic waves, these zones satisfy ideal resonance conditions, producing the most pronounced amplification. This finding has critical implications for seismic engineering practice: site classification and risk zoning in thick sediment areas cannot rely solely on thickness. Identification of hard interlayer locations and velocities through boreholes or microtremor array methods is essential to avoid systematic underestimation of actual amplification effects.

Based on site vulnerability index distribution, the study area can be classified into three risk zones (Figure 7). Extremely high-risk zones ($K \geq 60$) are located in the western thick sediment-multi-layer aquifer superposition belt. We recommend that new lifeline projects (hospitals, schools) increase seismic fortification intensity or adopt pile foundations with ground improvement. These areas are also high-risk zones for secondary disasters (sand boils, ground subsidence), requiring specialized liquefaction potential assessment. Moderate-risk zones (K = 20-60) cover the central 100-200 m thickness belt, where ordinary buildings can follow current design codes. Low-risk zones ($K < 20$) in the northeastern bedrock outcrop area require standard fortification and are suitable locations for regional emergency shelters.

5.3 Seismogenic Structure and Site Effects of the Guye *M*s 5.1 Earthquake

The 2020 *M*s 5.1 Guye earthquake on July 12 is a late aftershock of the 1976 great Tangshan earthquake, and its seismogenic structure belongs to the Tangshan Fault zone (Wang et al., 2024). After the 1976 event, the released stress was not confined to the source region, but diffused along the fault zone to the surrounding areas. The northern Tangshan region is characterized by extremely thin or even

absent sedimentary layers, which lack unconsolidated media to absorb and dissipate seismic wave energy. Consequently, stress tends to concentrate at fault tips and tectonically weak zones, triggering subsequent seismic activity (Li et al., 2007). The Guye earthquake occurred in the thin-sediment zone on the northern side of the same seismogenic fault as the great 1976 Tangshan earthquake, where the sediment thickness is only 40-80 m. However, the site vulnerability index in the epicentral area reaches 30-60, corresponding to a moderate-to-high vulnerability level. The site amplification factor exceeds 7.0, and prominent amplification is observed in the northern and eastern parts of the epicentral region, which is distinctly higher than that in surrounding areas with similar sediment thickness. This not only indicates that the thin-sediment zone near the fault tip may generate stronger ground shaking under the combined effect of stress concentration and site conditions, but also explains why the intensity V zone of the *M*s 5.1 Guye earthquake was concentrated in small areas to the southeast and north of the epicenter, forming an anomalous seismic damage zone (Li et al., 2020).

5.4 Legacy Effects of the 1976 Tangshan Earthquake Surface Rupture on Site Effects

The Tangshan earthquake occurred on the Tangshan Fault Zone within the Tangshan rhombic block (Guo et al., 1977). The Tangshan Fault Zone consists of the Tangshan–Guye, Tangshan–Douhe, and Weishan–Changshan faults, and the surface rupture exhibited right-lateral strike-slip characteristics (Zhang et al., 1980; Liu et al., 1982). Site parameters differ significantly across the fault zone: the thickness difference between the Tangshan–Douhe Fault and Weishan–Changshan Fault is <50 m with K generally <30, whereas the southwestern thick-sediment zone shows K >60. Heavier damage was observed near the Tangshan–Douhe Fault, which has shown no significant activity since the Late Pleistocene. A linear zone of anomalous seismic damage exists west of the Tangshan–Douhe Fault, where the northwestern side displays a high-damage belt with mortality rates significantly higher than the southeastern side; the anomaly boundary coincides with the Tangshan–Douhe Fault (Liu, 2014). We infer that the fault acted as a barrier to seismic wave propagation during the Tangshan earthquake, preventing rupture extension northeastward and causing energy to be repeatedly reflected and amplified in the thick sediments on the southwestern side, thereby exacerbating damage there.

This study obtained high-resolution site effect parameters for the Guye source zone using the HVSR method, but limitations remain: (1) The one-dimensional horizontal layered medium assumption cannot fully characterize the complex fault architecture and lateral heterogeneity of the Yanshan–North China Basin transition zone, potentially causing deviations in peak frequency and amplitude. (2) Shear

wave velocities were based on empirical values rather than station-specific measurements, and velocity errors systematically propagate to thickness inversion results. (3) HVSR peak amplitudes reflect only the lower bound of linear amplification without accounting for nonlinear soil responses, limiting applicability to small and distant earthquakes—corrections are required for large earthquake near-field assessments.

6. Conclusions

This study obtained high-resolution sediment thickness distribution and site effect characteristics in the Guye seismic source zone of Tangshan through a dense seismic array and the HVSR method.

(1) Sediment thickness in the study area ranges from 0-450 m, showing a spatial pattern of thin in the north and east, thick in the south and west, which aligns closely with the tectonics of the Yanshan Uplift–North China Rift Basin transition zone. The thickest deposits occur at the edge of the Tangshan Depression in the southwest, while bedrock is widely exposed along the southern margin of the Yanshan Uplift in the northeast. The clear gradient in thickness variations delineates differential movement of Quaternary active faults.

(2) Using the lognormal distribution and frequency-domain window-rejection algorithm, environmental noise interference was effectively suppressed, yielding more stable predominant frequencies (Cox et al., 2020). Site amplification factors in the study area range from 1.0-14.0, with high-value zones (A > 7.0) not occurring in the thickest sediment centers but rather concentrated in moderate-thickness zones, revealing the suppression mechanism of hard interlayers on amplification effects in deep sediment layers.

(3) The site vulnerability index in the study area shows a zonal characteristic of high values in the west and low values in the east (Figure 7), strongly coupled with sediment thickness and underground fluid systems. The western thick-sediment zone (K > 60), characterized by high porosity, multi-layer confined aquifers, and strong ground motion amplification, constitutes a superposition zone of extremely high building risk and liquefaction-induced secondary disasters, where seismic fortification intensity should be increased or sites avoided. Central areas (K = 20-60) require enhanced building seismic capacity, while the northeastern bedrock zone (K < 20) has relatively low risk where standard fortification measures are sufficient.

(4) The 2020 Guye *Ms* 5.1 earthquake occurred in a thin-sediment zone on the northern segment of the Tangshan Fault Zone, where high site amplification factors (A >7.0) coupled with fault activity

produced anomalous seismic damage under stress concentration. This demonstrates that site classification near fault zones cannot rely on single indicators and must consider the combined effects of fault fracture zones and stress concentration is sufficient.

The combination of dense arrays and the HVSR method not only reveals fine sedimentary structures inaccessible to previous drilling but also quantitatively assesses site damage potential and identifies potential seismic damage anomaly zones. This promotes the transition of regional seismic fortification from homogeneous approaches to site-fault coupling refinement, providing scientific support for resilient city construction.

Acknowledgments

We thank the Hebei Earthquake Agency for providing waveform data.

Author contributions

All authors contributed to the preparation, review, and editing of the manuscript. Y.X. was responsible for the writing of the manuscript. R.W. was responsible for waveform processing, calculating sediment thickness and site effects, and analyzing results. J.H. reviewed and revised the manuscript and provided constructive feedback. Y.W. validated the results and reviewed and edited the core academic content. X.W. provided the data and offered guidance on methodology and analytical framework. Y.Z. provided the core processing code for the HVSR method and also delivered critical technical support and methodological guidance for the conduct of this study. Z.J. was responsible for language translation of the manuscript. P.G. reviewed and revised the reference formatting.

Funding

This research is financially supported by the Earthquake Science Spark Program of Hebei Province (Grant Numbers DZ2025081900032), Science and Technology Innovation Program for Postgraduate students in IDP subsidized by Fundamental Research Funds for the Central Universities (Grant Numbers ZY20250307), National Natural Science Foundation of China (Grant Numbers 42174074, 41674055 and 42364006), and Hebei Natural Science Foundation (Grant Numbers D2025512035).

Data Availability

The station observation data were provided by the Earthquake Administration of Hebei Province, China.

Declarations

Competing interests

The authors declare no competing interests.

References

Ansal A, İyisan R, Yıldırım H (2001) The cyclic behaviour of soils and effects of geotechnical factors in microzonation. Soil Dynamics and Earthquake Engineering 21(5), 445–452. https://doi.org/10.1016/S0267-7261(01)00026-4

Bao F, Li ZW, Tian BF, Wang LL, Tu GH (2019) Sediment thickness variations of the Tangshan fault zone in North China from a dense seismic array and microtremor survey. Journal of Asian Earth Sciences 185:10405–10415. https://doi.org/10.1016/j.jseaes.2019.10405

Bard PY (1999) Microtremor measurements: A tool for site effect estimation. In: Irikura K, Kudo K, Okada K, Sasatani T (eds) The effects of surface geology on seismic motion, vol 3. Balkema, Rotterdam, pp 1251–1279

Chen QF, Liu LB, Wang WJ, Rohrbach E (2008) Mapping site response in Beijing urban area using microtremor. Chinese Science Bulletin 53(18):2229–2235

Cox BR, Cheng TJ, Vantassel JP, Manuel L (2020) A statistical representation and frequency-domain window-rejection algorithm for single-station HVSR measurements. Geophysical Journal International 221(3):2170–2183. https://doi.org/10.1093/gji/ggaa119

Feng P (2013) Tangshan engineering geological layer set in the key areas divided into research. Dissertation, Shijiazhuang University of Economics

Flores-Estrella H, Yussim S, Lomnitz C (2007) Seismic response of the Mexico City Basin: A review of twenty years of research. Natural Hazards 40(2):357–372. https://doi.org/10.1007/s11069-006-0034-6

Gao Y, Zheng SH, Sun Y (1995) Crack-induced anisotropy in the crust from shear wave splitting observed in Tangshan region, North China. Acta Seismologica Sinica 8(3):351–363

Guo SM, Li ZY, Cheng SP, Chen XC, Chen XD, Yang ZE, Li RC (1977) Discussion on the regional structural background and the seismogenic model of the Tangshan earthquake. Scientia Geologica Sinica 4:305–320

Haghshenas E, Bard PY, Theodulidis N, SESAME-Working-Team (2008) Empirical evaluation of microtremor H/V spectral ratio. Bulletin of Earthquake Engineering 6:75–108. https://doi.org/10.1007/s10518-007-9058-x

Holzer TL (1994) Predicting earthquake effects-learning from Northridge and Loma Prieta. Science 265(5176):1182–1183. https://doi.org/10.1126/science.265.5176.1182

Hunter JA, Crow HL (2012) Shear wave velocity measurement guidelines for Canadian seismic site characterization in soil and rock (Geological Survey of Canada Open File 7078). Geological Survey of Canada. https://doi.org/10.4095/291753. Accessed 20 March 2026

Ibs-von Seht M, Wohlenberg J (1999) Microtremor measurements used to map thickness of soft sediments. Bulletin of the Seismological Society of America 89(1):250–259. https://doi.org/10.1785/BSSA0890010250

Lachetl C, Bard PY (1994) Numerical and theoretical investigations on the possibilities and limitations of Nakamura's technique. Journal of Physics of the Earth 42(5):377–397. https://doi.org/10.4294/jpe1952.42.377

Lermo J, Chávez-García FJ (1994) Are microtremors useful in site response evaluation? Bulletin of the Seismological Society of America 84(5):1350–1364

Li CY, Wang YP, Wang ZC (2007) Some analyses on relation between the upper offset point and latest activity times of buried faults in cities of eastern China: Taking the Xingtai and Tangshan earthquake regions as an example. Seismology and Geology 29(2):431–445

Li XJ, Li N, Wang YS (2020) Information and enlightenment from the M5.1 Guye, Tangshan earthquake on 12th July, 2020. Progress in Earthquake Sciences 50(7):1–8. https://doi.org/10.3969/j.issn.2096-7780.2020.07.001

Liu BJ, Zhang XK, Chen Y, Feng SY, Ji JF, Yuan HK, Zuo Y (2011a) Research on crustal structure and active fault in the Sanhe-Pinggu Earthquake (M8.0) Zone based on single-fold deep seismic reflection and shallow seismic reflection profiling. Chinese Journal of Geophysics 54(5):1251–1259. https://doi.org/10.3969/j.issn.0001-5733.2011.05.014

Liu BJ, Qu GS, Sun MX, Liu K, Zhao CB, Xu XW, Feng SY, Kou KM (2011c) Crustal structures and tectonics of Tangshan earthquake area: Results from deep seismic reflection profiling. Seismology and Geology 33(4):901–912. https://doi.org/10.3969/j.issn.0253-4967.2011.04.014

Liu G, Guo S, Liu C (1982) Seismogeologic background. In: Liu G (ed) 1976 Tangshan Earthquake. China Seismological Press, Beijing, pp 71–130

Liu K, Zhang XW, Li JJ, Ma CQ, Zhang Y, Wang JP (2014) A discussion on the relationship between seismic damage distribution and geological structure of Tangshan earthquake. Journal of Catastrophology 29(2):25–28. https://doi.org/10.3969/j.issn.1000-811X.2014.02.006

Liu YY, Chong JJ, Ni SD (2011b) Near surface wave velocity structure in Chinese capital region based on borehole seismic records. Acta Seismologica Sinica 33(3):342–350. https://doi.org/10.3969/j.issn.0253-3782.2011.03.007

Long Z (2010) Quaternary lithostratigraphy and chronostratigraphy division and correlation in Tangshan urban area. Dissertation, China University of Geosciences, Beijing

Nakamura Y (1989) A method for dynamic characteristics estimation of subsurface using microtremor on the ground surface. Quarterly Reports of the Railway Technical Research Institute 30(1):25–33

Nakamura Y (1997) Seismic vulnerability indices for ground and structures using microtremor. In: World Congress on Railway Research. Florence, Italy, pp 1–7

Nakamura Y (2000) Clear identification of fundamental idea of Nakamura's technique and its applications. In: Proceedings of the 12th World Conference on Earthquake Engineering, Paper No. 2656. Auckland, New Zealand

Nogoshi M, Igarashi T (1971) On the amplitude characteristics of microtremor, Part II. Journal of the Seismological Society of Japan 24:26–40

Parolai S, Bormann P, Milkereit C (2002) New relationships between Vs, thickness of sediments, and resonance frequency calculated by the H/V ratio of seismic noise for the Cologne area (Germany). Bulletin of the Seismological Society of America 92(6):2521–2527. https://doi.org/10.1785/0120010248

Peng F, Wang WJ, Kou HD (2020) Microtremor H/V spectral ratio investigation in the Sanhe-Pinggu area: Site responses, shallow sedimentary structure, and fault activity revealed. Chinese Journal of Geophysics 63(10):3775–3790. https://doi.org/10.6038/cjg2020O0025

Pileggi D, Rossi D, Lunedei E, Albarello D (2011) Seismic characterization of rigid sites in the ITACA database by ambient vibration monitoring and geological surveys. Bulletin of Earthquake Engineering 9:1839–1854. https://doi.org/10.1007/s10518-011-9292-0

SESAME (2004) Guidelines for the implementation of the H/V spectral ratio technique on ambient vibrations measurements, processing and interpretation

(EVG1-CT-2000-00026). European Commission, Research General Directorate. http://sesame.geopsy.org. Accessed 20 March 2026

Su YK, Kim KH, Chiu JM, Liu L (2020) Microtremor HVSR analysis of heterogeneous shallow sedimentary structures at Pohang, South Korea. Journal of Geophysics and Engineering 17(1):1–9. https://doi.org/10.1093/jge/gxaa035

Walling MY, Mohanty WK, Nath SK, Mitra S, John A (2009) Microtremor survey in Talchir, India to ascertain its basin characteristics in terms of predominant frequency by Nakamura's ratio technique. Engineering Geology 106(3–4):123–132. https://doi.org/10.1016/j.enggeo.2009.03.013

Wang S, Li Z (2018) S-wave attenuation of the shallow sediments in the North China basin based on borehole seismograms of local earthquakes. Geophysical Journal International 214(2):1391–1400. https://doi.org/10.1093/gji/ggy223

Wang TL, Zhang SZ, Cui BW, Wang XS, Liu XY (2024) Microearthquake detection and seismicity analysis of the 2020 Guye Ms5.1 earthquake sequence. Chinese Journal of Geophysics 67(4):1501–1514. https://doi.org/10.6038/cjg2023Q0865

Wang W, Chen Q, Chen L (2012) Review on near-surface soft structure investigation with seismic noise. Earthquake Research in China 28(4):335–350. https://doi.org/10.3969/j.issn.1001-4683.2012.04.001

Wen RZ, Wang HW (2020) Strong-motion recordings in Ms5.1 Guye, Tangshan earthquake on July 12, 2020. Progress in Earthquake Sciences 50(7):9–13. https://doi.org/10.3969/j.issn.2096-7780.2020.07.002

Yu YY (2016) Research on seismic effects of three-dimensional sedimentary basins. Dissertation, Institute of Engineering Mechanics, China Earthquake Administration

Zhang Z, Li Q, Gu J, Xu X, Wang M (1980) The fracture processes of the Tangshan earthquake and its mechanical analysis. Acta Seismologica Sinica 2(2):111–129